

STUDY ON RADAR DIFFERENTIAL INTERFEROMETRY TECHNOLOGY AND IT'S APPLICATION TO MANI EARTHQUAKE USING ERS-1/2 SAR DATA: A CASE STUDY IN CHINA

Qulin Tan ^{a,*}, Siwen Bi ^b, Bin Wang ^a, Songlin Yang ^a

^a School of Civil Engineering & Architecture, Beijing Jiaotong University, Beijing, 100044, China - qulintan@sina.com

^b Institute of Remote Sensing Applications, CAS, Beijing, 100101, China – bisw@irsa.irsas.ac.cn

KEY WORDS: SAR, Earthquakes, Recognition, Mapping, Measurement, Change Detection

ABSTRACT:

Mani Earthquake, occurred on Nov. 8, 1997 in Tibet, China, is the strongest event in China since 90's in 20 century. Investigation and research of its principle and geometry, dynamics related to surface rupture zone is very significant to analyze the development and evolution of China's earthquake in the future. In this study, we investigate the distribution of surface deformation and extract displacement information of the earthquake rupture zone using differential SAR (ERS1/2 SAR) interferometry. The data set related to our study area are ERS1/2 SLC SAR images (April 15, April 16, 1996 ERS-1 and Dec. 2, 1997 ERS-2) provided by European Space Agency. We analyzed factors related to the surface deformation detecting interferogram along the Margaichace-Ruolacuo fault under the special regional environmental conditions. From the changing interferogram, we concluded that the zone around Margaichace-Ruolacuo fault is the most severely deformed and the most possibly rupturing area; epicenter is located in this zone. Also we concluded from analyzing the fringe patterns that left-lateral shear movement is the whole deforming mechanism, furthermore, the offsets are also quantitatively estimated. We inferred that the horizontal offset displacement for the southern side at least reaches 2.8m and 1.75m at least for the northern side of the fault. All these results agree well with the slip measured in the field, with the displacement measured by surveying, and with the results of an elastic dislocation model.

1. INTRODUCTION

Radar differential interferometry is an up-to-date measurement technology. It is now possible to detect subtle changes in the Earth's surfaces over periods of days to years with a scale (global), accuracy (millimeters), and reliability (day or night, all weather) that are unprecedented. The basic principle of the technique involves interferometric phase comparison of a series of SAR images. To date many examples illustrate how SAR differential interferometry can be applied to the study of coseismic deformation generated by an earthquake (Gabriel A. K, Goldstein R. M. and Zebker H. A. 1989; Gens R, Genderen V. J. 1996). Because of its unique capability, which no other technique provides high-spatial-resolution maps of earthquake deformation, these pioneering studies have generated enormous interest in the Earth science community because they point to an entirely new way to study the surface of the Earth.

Although the techniques are now well documented in the international literature, only an example of acquisition of high accuracy DEM using SIR-C interferometric data has been reported in China (Wang Chao, 1997). For short of interferometric data source, the application examples of SAR interferometry is few as a whole in China, and the case study of differential SAR interferometry for mapping surface deformation is further much less. Along with the development of radar remote sensing, more and more SAR interferometric data would be available and China will certainly receive its own independent interferometric data source in the future. So it has become increasingly important to understand the limitations of the processing and the acquisition method itself for Chinese geoscientists.

On the other hand, many Chinese geologic scientists are unfamiliar with SAR interferometry and its potential new applications, and its technical limitations need to be more fully explored. In an attempt to understand the principle and the influencing factors involved with repeat-pass space-borne SAR systems, such as the European Space Agency's ERS-1/2, I examined an area around Mani, a region in Tibet, China using SAR differential interferometry. In this paper, I will provide a brief description of the principle and processing steps, discuss the influencing parameters related to topography, and present the resultant changing interferogram calculated from the ERS-1/2 data. These are objectives of the study.

2. PRINCIPLE OF SAR DIFFERENTIAL INTERFEROMETRY

The development of differential SAR interferometry is based on SAR interferometry technique, and the interferometric data can be acquired by two antennae on the same platform, or by one antenna on "repeating" its orbit (Rodriguez E. 1992), and J. M. Martin. Because all space-borne SARs in run are single-band and single-antenna systems, many published literatures related to the technique have been used repeat-pass interferometric data.

If ignoring some parameters influencing the quality of SAR interferometric data, such as atmospheric differences at the two times of imaging, internal clock drift, weather conditions, system noise et al, we present the interferometer geometry and range difference attributable to three factors: 1) A spherical earth with no topography, 2) topography, and 3) surface

* Corresponding author.

deformation. If we can subtract phase gradients resulted from 1) and 2) on interferograms, then the information of residual phase gradients can be used to monitoring dynamic change of earth surface (Gabriel A. K, Goldstein R. M, 1989). According to the different methods of removing topographic effects, we can basically classify the technique into two categories: differential interferometry based on DEM simulated interferogram and differential interferometry based on unprimed SAR interferogram, but as to principles related to the two methods, there is no evident difference.

Consider the condition of no existence of surface deformation during SAR imaging period, the general geometry of SAR interferometry is illustrated in figure 1. Two radar antennas A_1 and A_2 simultaneously viewing the same surface and separated by a baseline vector B with length B and angle α with respect to horizontal. A_1 is located at height h above some reference surface. The distance between A_1 and the point on the ground being imaged is the range ρ , while $\rho + \delta\rho$ is the distance between A_2 and the same point. If λ is the wavelength of the radar and $\delta\phi$ is the range difference between the reference and repeat passes of the satellite, the phase difference ϕ between the signals received from the same surface element at the two antenna positions is:

$$\phi = \frac{4\pi}{\lambda} \delta\rho \quad (1)$$

Recalling the law of cosine, Eq. (2) can be easily obtained according to the imaging geometry.

$$(\rho + \delta\rho)^2 = \rho^2 + B^2 - 2\rho B \sin(\theta - \alpha) \quad (2)$$

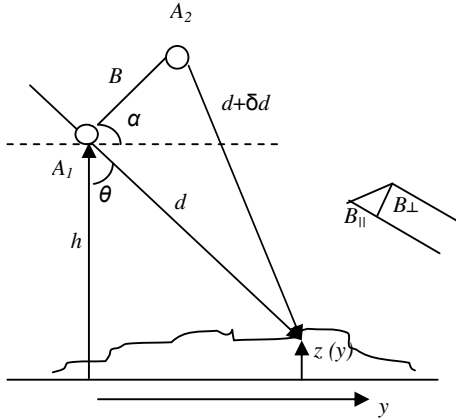


Figure 1. Imaging geometry of repeat-pass SAR interferometry

Where θ is the look angle of the imaging radar. For spaceborne geometries, we can make the parallel-ray approximation and rearrange the above equation by ignoring the second term $(\delta\rho)^2$ on the right-hand side of Eq. (2), thus we obtain:

$$\delta\rho \approx B \sin(\theta - \alpha) + \frac{B^2}{2\rho} \quad (3)$$

Because of $\rho \gg B$ we can discard the term of $\frac{B^2}{2\rho}$ for simplicity of analysis, thus we have another equation:

$$\delta\rho \approx B \sin(\theta - \alpha) = B_{\parallel} \quad (4)$$

where B_{\parallel} is the component of baseline parallel to the look direction.

Combining with Eq. (4), we can rearrange Eq. (1) as:

$$\phi \approx \frac{4\pi}{\lambda} B_{\parallel} \quad (5)$$

From equation (5), we know that the measured quantity of phase difference ϕ is directly proportional to B_{\parallel} and wave numbers $(2\pi/\lambda)$, with constant of proportionality 2.

On the assumption that we have the second interferogram (primed interferogram) over the same region with the same ρ and θ as the first interferogram (unprimed interferogram), but having a baseline length B' and angle α' with respect to horizontal, we can obtain the equation $B'_{\parallel} = B' \sin(\theta - \alpha')$ similar to Eq. (4). Similarly, we can obtain Eq. (6) similar to Eq. (5) on the condition that no factors other than topography generate phase effects.

$$\phi' = \frac{4\pi}{\lambda} B'_{\parallel} \quad (6)$$

Combining Eq. (5) with (6), when radar wavelength is constant we obtain:

$$\frac{\phi}{\phi'} = \frac{B_{\parallel}}{B'_{\parallel}} \quad (7)$$

Which means that, the ratio of the two phases is just equaled to the ratio of the two parallel components of the baseline, i.e., independent of topography.

Now consider the second interferogram acquired over the same region as before but at different time, so that ground deformation (due to an earthquake) has displaced many of the resolution elements for the primed interferogram in a coherent manner. In addition to the phase dependence on topography, this time there is an additional phase change due to the radar line-of-sight component of displacement $\Delta\rho$.

In the primed interferogram, the phase ϕ' is

$$\phi' = \frac{4\pi}{\lambda} (B'_{\parallel} + \Delta\rho) \quad (8)$$

The surface displacement $\Delta\rho$ adds to the topographic phase term, which could create confusion in the interpretation. However, if the data from the initial unprimed interferogram are properly scaled with a proportional factor $\frac{B'_{\parallel}}{B_{\parallel}}$ and subtracted from the primed interferogram, we can obtain a solution dependent only on $\Delta\rho$, as follows:

$$\phi' - \frac{B'_{\parallel}}{B_{\parallel}} \phi = \frac{4\pi}{\lambda} \Delta\rho \quad (9)$$

Since the quantity on the left is determined entirely by the phases of the interferograms and the orbit geometries, the line-of-sight component of the displacement $\Delta\rho$ is measurable for each point in the scene.

For operational use, a common method is that the baseline parameters of primed interferogram are used to simulate the unprimed interferogram derived from only topography effects, which then is subtracted from primed interferogram. The resulted differential interferogram contains only the information related to surface deformation.

It is important to assess the relative sensitivity of the phase measurement to topography and displacement since the topography itself may be poorly known. From the imaging geometry, it can be seen in Fig.1 that the height z of the point z (y) can be determined by:

$$z = H - \rho \cos \theta \quad (10)$$

where H is the flying height. The relative sensitivity of the phase may be derived by differentiating Eq. (10) with respect to θ :

$$dz = \rho \sin \theta d\theta \quad (11)$$

And also we can differentiate Eq. (8) with respect to θ and displacement $\Delta\rho$. Because of the irrelevance between $\Delta\rho$ and B'_{\parallel} and recalling Eq. (4), we can obtain Eq. (12) and Eq. (13):

$$d\phi' = \frac{4\pi}{\lambda} B' \cos(\theta - \alpha') d\theta \quad (12)$$

$$\frac{d\phi'}{d\Delta\rho} = \frac{4\pi}{\lambda} \quad (13)$$

For the displacement case, we have Eq. (13). Combining Eq. (11) with (12), we can obtain Eq. (14):

$$\frac{d\phi'}{dz} = \frac{4\pi B' \cos(\theta - \alpha')}{\lambda \rho \sin \theta} \quad (14)$$

Since baseline length (a few hundred meters) is much less than ρ (a few hundred kilometers for a spacecraft system), it is

evident from Equation (13) and (14) that $\frac{d\phi'}{dz}$ is much smaller

than $\frac{d\phi'}{d\Delta\rho}$. Thus, the measured phase is much less sensitive to

topography (Eq. (14)) compared to displacement (Eq. (13)). When the accuracy of measuring topography using SAR interferometry reaches the level of meter, the accuracy for measuring deformation displacement can reach the level of centimeter or Millimeter. Comparing the two results numerically for the case of ERS-1, 1 m of topography gives a phase signature of 4.3 degree (actually less than the real noise limit about 20 degree, implying that ERS-1 is not sensitive to topography at this level). However, for the same pass pair, a 1-m surface displacement yields a phase signature of 12,800 degree, or nearly 3000 times greater sensitivity. Since we seek to measure 1-cm surface changes, this implies that we require topographic data accurate to about $3000 \times 1\text{cm}$, or $\pm 30\text{m}$.

3. CASE STUDY

The Mani Earthquake occurred 10:02:55.4 a.m. (UTC) on Nov. 8, 1997 around 150km away from Mani country in Naqu region, Tibet, China. The location of epicenter is 87.33°E, 35.26°N, the depth of 40km, the magnitude of Ms7.4 measured by China earthquake observation network. Concerning the earthquake, the data measured by NEIC (National Earthquake Information Center of America) are that: time is 10:02:54.9 a.m. (UTC), location of epicenter is 87.37°E, 35.11°N, the depth of 35km, and the magnitude of Ms7.9 (Feng Hao, 1997).

Mani Earthquake is the strongest event in China since 90's in 20 century. Investigation and research of its principle and geometry, dynamics related to surface rupture zone is very significant to analyze the development and evolution of China's earthquake in the future. In this study, we investigate the distribution of surface deformation and extract displacement information of the earthquake rupture zone using differential SAR (ERS1/2 SAR) interferometry.

3.1 Site Background and Data Source

The epicenter of Mani earthquake is located the nearly east to west Margaichace-Ruolacuo fault zone along the northern boundaries of Qiang-Tang block, south of Chaoyang lake. The Margaichace-Ruolacuo fault extends approximately 270km and has experienced strong events since Holocene epoch. Remote sensing images around this area are characterized by less

disturbance, distinct and clear tectonic evidence because there exists scarce vegetation, uncovered surface, and dry atmospheric condition, and desolate and uninhabited around the area. For these potential advantages, this area has become the optimal region for using remote images to detect and investigate geological movement such as tectonics, fault, earthquake et al.

Jianhua Li (1998) analyzed 1:100 000 Landsat satellite images and recognized the Mani earthquake as active evidence of the Margaichace-Ruolacuo fault. On the remote sensing images, a series of valleys were distorted consistently along the Margaichace-Ruolacuo fault, evidently showing the fault features slipping along its trend. Around the Margaichace-Ruolacuo fault zone, linear fault reticule features are distinct and clear, evidently showing the appearance of left-lateral slipping movement. Measurement results have been reported that the maximum left-slip displacement of the first-level water system reaches 3500m (Li Jianhua, 1998).

The data set related to our study area are ERS1/2 SLC SAR images (April 15, April 16, 1996 ERS-1 and Dec. 2, 1997 ERS-2) provided by European Space Agency. There are two scenes for each imaging date, so there are six scenes in total for data processing related to the study.

3.2 Methods of Surface Deformation Mapping

The data processing procedure of differential SAR interferometry can be divided into two big steps. Firstly, performing registration between the two focusing SAR images acquired before and after surface deformation, then conjugating to generate the prime interferogram; Secondly, from the prime interferogram subtracting the unprimed interferogram generated from SAR images acquired before surface deformation or simulated interferogram generated from existing DEM, thus surface deformation interferogram is obtained.

The software for data processing in this study mainly related to using the EarthView Interferometric SAR Processor of Atlantis Scientific Inc. Canada. This processing software allows for the user feedback rectification of the parameters influencing resultant interferogram, and can meet the geoscientist's need for various geo-applications of SAR interferometry. The epicenter of Mani is just located between the two scenes of ERS image Frame 2889 and Frame 2907. So it is required to manipulate two set of SAR images, and then mosaic the two resultant interferogram.

The basic steps of InSAR data processing in our study can be presented as follows:

(1) Using the ERS-1 image acquired on April 15, 1996 as slave image and the ERS-2 image acquired on April 16, 1996 as master image, which form a tandem pair, then extracting the DEM of the study area.

(2) Using the ERS-2 image acquired on Dec. 2, 1997 as slave image and the same image of April 16, 1996 as master image, forming primed interferogram by multiplying each complex pixel in master image by the complex conjugate of the matching pixel in the slave image.

(3) Using the DEM generated from the first step, and the baseline parameters of the second processing step, generating the unprimed simulating interferogram.

(4) Finally, subtracting the unprimed interferogram from the primed interferogram, then obtaining differential deformation interferogram along slant range.

There are some data processing steps that are either done differently here than in previous studies or should be elaborated upon for the sake of explaining the resolution and interpretation of our results. These include re-estimation of baselines from twenty GCPs collected from 1:10,000 topographic map in order to improve the accuracy of DEM extraction (Kimura H, 1997), and flat phase removal method. The flat earth correction method using the EarthView Software removes those fringes due to earth curvature and imaging geometry reference to sea level. So this method leads to evidently residual phase gradient on the interferogram because the average altitude of study area is 5000m. In order to avoid evident errors in DEM and surface deformation information extraction, the residual phase gradient must be removed (Goldstein R. M, Zebker H. A, 1988). As to the topographic interferogram, the flat region in study area was selected to estimate the residual phase gradient. After removing the residual phase gradient, the topographic interferogram was unwrapped and then derived DEM, which RMS is 18.7m with comparison to 1:100 000 topographic map. For the deformation detection interferogram, the region far away from epicenter and with regular fringes was selected to estimate the residual phase gradient and then removed, where impossibly exist surface displacement.

Finally, the two resultant surface deformation detecting interferograms were mosaicked with the match errors within half of fringe (see Figure 2). From the mosaic interferogram, we can infer that the fringe errors of surface deformation detecting interferogram in this study, which derived from errors of topography and flat phase gradient, also lie within the level of accuracy.

3.3 Deformation Analysis Based on Differential Interferogram

The effects influencing interferometric data decorrelation, reported by Zebker (Zebker H. A. and Villasenor J, 1992), can be mainly attributed to these four factors: 1) baseline decorrelation; 2) additive noise/speckle; 3) temporal decorrelation for random phase component due to the complicated interference pattern produced by radar signal interaction with multiple ground scatterers within an image resolution element; 4) geometric decorrelation. In this study, we analyzed these factors related to the surface deformation detecting interferogram along the Margaichace-Ruolacuo fault, combining with the regional environmental conditions.

The derived deformation detecting interferogram show several areas of fringe disturbance (Figure 2), and the areas other than the area around Margaichace-Ruolacuo fault mostly are associated with lakes. Because the lake water is characteristic of seasonal variation, we inferred that the fringe disturbance associated with lakes area sound reasonable for lake-water backscattering decorrelation. This deformation could be either earthquake related or indicate a seasonal change of the lake-water between spring and summer.

One of the most significant sources of error in InSAR processing is that of phase noise. Atmospheric disturbances, thermal noise, baseline effects on correlation cause phase noise. We can essentially ignore the former in this area because of the intense dryness of the atmosphere. The second, thermal noise, is

a random error and, as such, is impossible to quantify at any given point. To reduce its effects, additive noise/speckle is depressed by multi-look SAR image processing. The third, baseline effects on correlation, is reduced by removing the flat phase. Concerning on topographic effects, although average altitude of the study area is high, but the relative height is within 600m, the layover and foreshortening appearances for existing steep hills on SAR images are relatively few. So the large extent of decorrelation area on interferogram may be attributed to temporal decorrelation, but it is impossible. Since that the study area is above 4800m altitude with rare vegetation cover and consists mainly of a series of Gobi and monadnocks, the backscattering variation between imaging dates should be less difference.

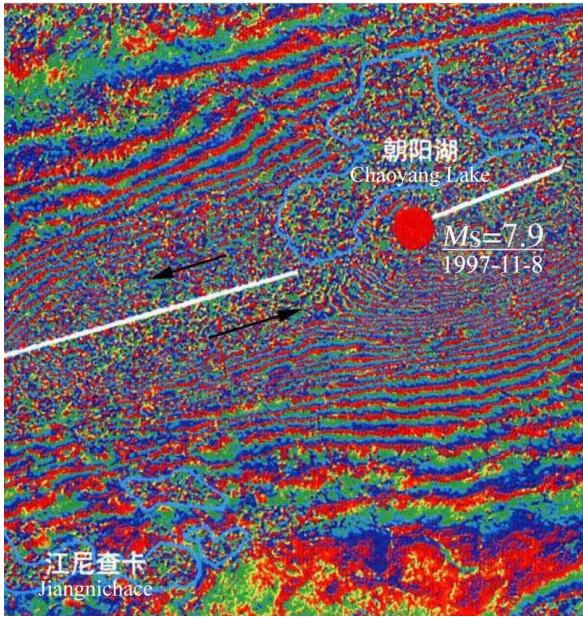


Figure 2. The changing interferogram of Mani Earthquake, Tibet on Nov. 8, 1997

According to above analysis of influencing effects, we can conclude that the fringe disturbance around the Margaichace-Ruolacuo fault zone exclusively attribute to effects for surface deformation, which is exceeded the range SAR interferometry can measure. A step further, we infer from the differential InSAR interferogram that the slips or block offsets, along secondary fractures within the main rupture around the Margaichace-Ruolacuo fault zone, bring in the fringe disturbance and displacement field decorrelation. In summary, analyzing the resultant deformation interferogram, we draw a conclusion that the area around the Margaichace-Ruolacuo fault is the ultimately possible surface rupture zone and is the most severe deformation area; epicenter also is located in this zone.

The fringe pattern around the Margaichace-Ruolacuo main rupture is dense and elongated parallel to the azimuth of the rupture. The density of fringes decreases logarithmically across the rupture from near to faraway as is expected from elastic half-space modeling of the lithosphere. Because of asymmetric fringes distribution along the two sides of the fault, this pattern is indicative of a left-lateral horizontal shear in the direction of earthquake rupture (Peltzer, G. and P. Rosen, 1995). If no vertical deformation and only horizontal shifts parallel to the

azimuth of the rupture are assumed, this evidence, combined with the viewing geometry mentioned above, indicates that the ratio of deformation displacements along radar viewing direction to the presumed direction, is equal to $\sin\phi\sin\theta \approx 0.32$, where $\theta \approx 23^\circ$ is the radar incidence and $\phi \approx 70^\circ$ is the angle between the nadir trace of radar and the presumed deformation offset direction. So we can obtain the horizontal offsets using the deformation displacement along the radar viewing direction by dividing the value of 0.32. Under the presumption, if the relative displacement of horizontal offset between two neighboring pixel exceeds $\delta = 2.8/0.32 = 8.75$ cm, the displacement along radar viewing direction will exceeds the range one fringe cycle can measure on differential interferogram, and fringe disturbance will be emergent. On the resultant interferogram of this study, the southern side of the fault from disturbance area outward exists at least 32 fringes, and the northern side of the fault from disturbance area outward exists at least 20 fringes. We can infer that the horizontal offset displacement for the southern side at least reaches 2.8m and 1.75m at least for the northern side of the fault. Apparently, the deformation displacement in the southern side is more severe than that in the northern side. But it should be pointed that horizontal left-lateral shear in the direction of earthquake rupture is the whole surface deformation form, as to some local points there maybe exist vertical deformation components, and also maybe superimpose the later shifts. For example, near the epicenter area maybe superimpose subsidence after earthquake because the southern fringes of epicenter show evidently curves of arc.

Field observations by Xu Xiwei (China National Earthquake Agency's Staff, 2000) manifest that the surface rupture zone of Mani earthquake in uninhabited area of northern Tibet lies in the northern boundary around the Margaichace-Ruolacuo fault fracture zone. The nearly vertical rupture zone is the seismic fault of Mani earthquake, trending NE-E direction, extending 120km long and 300~400m in width. The nature of fault movement is dominant by left-rotary shear with the maximum displacement 4.5m and the horizontal shift along its east and west sides is about 2~3m. This agrees with the mapping results obtained by analyzing the differential interferogram around Mani earthquake area.

Another research by Xu Lishen et al. (1999) also points that the seismic fault of Mani earthquake is a left-rotation reverse fault rupturing from west to east, trending 250° direction, and the tilt angle is nearly vertical, about 88° (Xu Lisheng and Chen Yuntai, 1997). Their research concludes that Mani earthquake, on the whole, is characterized by single-side rupturing. All these conclusions, at some extent, agree with the analysis results from differential interferogram.

4. CONCLUSIONS

With ERS-1/2 SAR data set, we use differential SAR interferometry to capture the co-seismic displacement field produced by the Mani earthquake occurred on Nov. 8, 1997 in Tibet, China. From the changing interferogram, we concluded that the zone around Margaichace-Ruolacuo fault is the most severely deformed and the most possibly rupturing area. Also we concluded from analyzing the fringe patterns that left-lateral shear movement is the whole deforming mechanism and furthermore the offsets are also quantitatively estimated. The

observed changes in range from the ground surface to the satellite agree well with the slip measured in the field, with the displacement measured by surveying, and with the results of an elastic dislocation model.

With suitable SAR data set and processing methods, SAR differential interferometry can capture high-spatial-resolution co-seismic displacements and surface deformation information on the order of centimeters, without advance knowledge of the earthquake's location by removing the signal from the topography. But it is notified that fringe indications on the differential interferogram represent only the shift of every pixel along radar viewing direction, the actually surface deformation displacement maybe trend vertical or horizontal direction, or slant direction, furthermore maybe the comprehensive deformation displacement along various direction. Thus, the deformation interpretation of the differential interferogram and fringe patterns could be various. Our observations show that there is localized heterogeneity in the deformation field of the Mani earthquake within 270 km of the main rupture. This discrepancy could be resolved with further modeling of the displacement expected from an elastically responding lithosphere and comparison of models to interferometric results.

Radar differential interferometry has generated enormous interest in the China's Earth science community because they point to an entirely new way to study the surface of the Earth, it is grandly significant to earth sciences, especially to seismology studies. Also it will become an essential technological method to monitor, assess, and relieve earthquake activity, combining with GPS, imaging-spectral sensor, and thermal infrared sensor et al. remote sensing new technologies. It is expected that the technique and its applications of SAR differential interferometry will develop rapidly with the development of radar remote sensing in China.

REFERENCES

- Feng Hao, 1999. Discussion on the Magnitude of the Earth quake Occurring at Mani, Tibet on November 8, 1997. *Recent Developments in World Seismology (Chinese)*, (7), pp. 1~7.
- Gabriel A. K, Goldstein R. M. and Zebker H. A., 1989. Mapping small elevation changes over large areas: Differential radar interferometry. *J. Geophys. Res.*, 94(B7), pp. 9183~9191.
- Gens R, Genderen V. J., 1996. SAR interferometry-issues, techniques, applications. *Int. J. Remote Sensing*, 17(10), pp. 1803~1835.
- Goldstein R. M, Zebker H. A. and Werner C. L., 1988. Satellite radar interferometry: two-dimensional phase unwrapping. *Radio Sci.*, 23(4), pp. 713~720.
- Kimura H., and M. Todo, 1997. Baseline Estimation Using Ground Points for Interferometric SAR. *IGRASS'97*, pp.442~444.
- Li Jianhua., 1998. A study on fault activity of Qiangtang and its neighboring areas in Tibet by using Landsat Images. *Seismology and Geology (Chinese)*. 20(3), pp. 201~207.
- Peltzer, G. and P. Rosen, 1995. Surface displacement of the 17 May 1993 Eureka Valley, California earthquake observed by SAR interferometry, *Science*, 268, pp. 1333-1336.

Rodriguez E., and J. M. Martin., 1992. Theory and design of interferometric synthetic aperture radars. *IEEE, Proceedings-F*, 139(2), pp. 147-159.

Xu Lisheng and Chen Yuntai, 1999. Earthquake rupture process of the 1997 Mani, in Tibet, China, *Acta Seismologica Sinica (Chinese)*, 21(5), pp. 449~459.

Xu Xiwei, Song Fangming, Yang Xiaoping et al., 2000. Seismological evidences and implications of potential earthquake source around surface rupture region in China. *Research on earthquake information (Chinese)*, 44(1), pp. 14~26.

Zebker H. A, Rosen P, Goldstein R. M, et al., 1994. On the derivation of coseismic displacement fields using differential radar interferometry: The Mani earthquake. *J. Geophys. Res.*, 99, pp. 19617~19634.

Zebker H. A. and Goldstein R. M., 1986. Topographic mapping from interferometric synthetic aperture radar observations, *J. Geophys. Res.*, 91(B5), pp. 4993~4999.

Zebker H. A. and Villasenor J., 1992. Decorrelation in interferometric radar echoes. *IEEE Trans. Geosci. Remote Sensing*, 30(5), pp. 950~959.

ACKNOWLEDGEMENTS

The project is supported by the Foundation (Grant No. SK040002) of State Key Laboratory of Remote Sensing Sciences, CAS and the NJTU Intellectual Foundation of China (Grant No. TJJ03002).